Additive Manufacturing 114 (2025) 105038

Contents lists available at ScienceDirect

Additive Manufacturing

journal homepage: www.elsevier.com/locate/addma

High-performance electromagnetic micropumps fabricated via multi-material jetting additive manufacturing

Chen Lin [a], Xu Chen [a], Zeyu Wang [a], Xiaotong Guo [a], Michail E. Kiziroglou [a,b,*], Eric M. Yeatman [a,c,*]

[a] Department of Electrical and Electronic Engineering, Imperial College London, Exhibition Road, London SW7 2AZ, United Kingdom
[b] Department of Industrial Engineering and Management, International Hellenic University, 14th km, Thessaloniki 57001, Greece
[c] College of Science and Engineering, University of Glasgow, University Avenue, Glasgow G12 8QQ, United Kingdom

ARTICLE INFO

Keywords:
Micropump
3D printing
Electromagnetic micropump
Polyjet
Viscoelastic

ABSTRACT

Micropumps serve as key sources of liquid propulsion in various microfluidic applications. High-performance with low fabrication complexity and cost is vital for disposable applications and mass production but remain challenging for electromagnetic reciprocating micropumps. Multi-material jetting (MMJ) 3D printing offers an opportunity owing to multi-material integration and high production efficiency while maintaining satisfactory resolution and surface quality for pump performance. However, there has been no previous demonstration of efficient fabrication of cost-effective liquid passive-valve electromagnetic micropumps based on MMJ 3D printing or other additive manufacturing techniques due to challenges in 3D model design and tailored fabrication workflow. This work proposes a new 3D model design to allow high-quality integration of soft and rigid elements and facilitate efficient assembly with good sealing based on a tailored fabrication workflow. Experimental optimization of micropumps is performed by comparing the performance of prototypes with varying chamber volume and membrane thickness. The devices are magnetically actuated wirelessly and exhibit a maximum flow rate and backpressure of 8.7 mL/min and 5.9 kPa at 1 W actuation power for a pump diaphragm diameter of 8 mm. Low material cost, estimated to be 1.1 £ per micropump, has been achieved. The membrane's viscoelastic behavior during operation is characterized. Flow rate stability tests show the coefficient of variation down to 6–11 % for an instant flow rate ranging from 4 to 7 mL/min, indicating feasibility in practical applications. These results suggest the great promise of MMJ 3D printing for low-cost, high-performance, miniature micropumps suitable for low-voltage disposable applications and mass production.

1. Introduction

Micropumps are miniature devices serving as propulsion sources for distributing liquid and gas, significant for microfluidic applications such as fluidic actuation, drug delivery, and biological analysis [1]. The general requirements for micropumps include small size, compactness, low cost, low power consumption, fluid-type compatibility, and controllable flow rate for target applications [2]. As a prevalent group of micropumps, reciprocating micropumps show the advantages of high precision, wide fluid-type compatibility, self-priming, and high-pressure output, making them useful in microfluidic and biomedical applications [3,4].

In the family of reciprocating micropumps, electromagnetic reciprocating micropumps are attractive because of low operation voltage, wireless actuation, fast response, and high flow rate. Moreover, they show relatively low fabrication difficulty and cost, vital for disposable applications and mass production [4,5], owing to the compatibility with polymer material and fabrication process [5]. Nonetheless, the optimization of their size, fabrication complexity, and cost is still challenging due to elaborate fabrication procedures for check valves, micropump housing, and membrane integration. Previously reported methods were based on molding and layer bonding. For example, Pan et al. [6] used a molding process to fabricate the polydimethylsiloxane (PDMS) housing and thermal bonding to connect the PDMS membrane and encapsulating layer to the chamber housing. They also demonstrated a simple fabrication method for ball check valves using heat-shrink tubes and micropipette tubes, though much labor was required for tube preparation and assembly. Shen et al. [7] used seven layers of polymethyl

* Corresponding authors at: Department of Electrical and Electronic Engineering, Imperial College London, Exhibition Road, London SW7 2AZ, United Kingdom.
E-mail addresses: m.kiziroglou@imperial.ac.uk (M.E. Kiziroglou), e.yeatman@imperial.ac.uk, eric.yeatman@glasgow.ac.uk (E.M. Yeatman).

https://doi.org/10.1016/j.addma.2025.105038
Received 6 July 2025; Received in revised form 17 October 2025; Accepted 28 November 2025
Available online 29 November 2025
2214-8604/© 2025 The Authors. Published by Elsevier B.V. This is an open access article under the CC BY license (http://creativecommons.org/licenses/by/4.0/).

methacrylate (PMMA) sheets and one cured PDMS membrane to fabricate their micropump, with a hot press process for 5 min per layer. The PMMA sheets and plates were fabricated using precision milling tools and the powder blasting technique. Mi et al. [8] introduced a minimized design of a valveless (diffuser-nozzle type) electromagnetic micropump that allows all layers to be fabricated by soft lithography and thermal bonding to integrate all layers and a miniature electromagnetic coil. In these works, the fabrication methods involve PDMS molding, high-precision photomasks, photolithography, and multiple-layer aligning and bonding, which increases consumables and labor costs and also the negative impact of extensive manual processes.

Pioneer research has been conducted to reduce the fabrication complexity and cost of electromagnetic reciprocating micropumps using additive manufacturing. Some researchers have exploited fused filament fabrication (FFF), also known as the fused deposition modeling (FDM) method. For example, Thomas et al. [9] used FDM to print the channels and the chamber for a diffusor micropump with polylactic acid (PLA) plastic material. Before being bonded to the 3D-printed component, Fe-PDMS composite membranes were fabricated separately by mixing PDMS solution and Fe particles. Their success marks the feasibility of 3D printing for valveless micropumps. Nonetheless, further miniaturization, actuation efficiency, flow rate range, and the repeatability of rectification performance are constrained by the diffuser-nozzle structure and FDM. Taylor et al. [10] proposed a set of process flows for FFF-printed pumps, including multiple times of pausing the 3D printer for object removal and manual assembly, enabling relatively quick and low-cost fabrication of magnetically actuated ball-valve pumps for liquid. The membrane was a thin layer of Nylon 12 with good chemical properties and mechanical strength. To improve performance, they designed compact magnetic pumps based on special side-to-side actuation of a Nylon 12 membrane [11] and achieved a valveless design by diffusers and peristaltic flow. Their work showed pumps with impressive flow rates under high-frequency actuation by a rotating magnet. Nonetheless, the fabrication workflow becomes less efficient for larger batch amounts, and the special working principle based on the swing of a large cylinder magnet may produce collision noise and instability.

Though proved effective, the general limitations of FDM in micropump fabrication such as printing speed, printing quality (resolution, surface quality, etc.), and requirement for elaborate integration, make the exploration of alternative approaches attractive. Photopolymerization technologies, such as stereolithographic (SL or SLA) and digital light processing (DLP) were applied and initially tested for the fabrication of microchannels, microvalves, and pneumatic peristaltic pumps [12–14]. Harnessing the high resolution of photopolymerization, valveless micropumps with various miniature rectification structures were fabricated using micro-stereolithography (PμSL) 3D printing. For example, Huang et al. [15] fabricated 3D vortex tube diodes with an axial tube diameter of 0.25 mm for rectifying flow. Similarly, Zhou and coworkers [16] fabricated periodic tetrahedron channels using PμSL for rectification and showed a difference in forward and backward flow. Many other asymmetrical structures have been designed and demonstrated on larger scales and are potentially printable by SLA and DLP [17]. However, better rectification performance and addressing negative flow fluctuation for low-frequency actuation, such as electromagnetic actuation [17], are still under investigation to improve the performance of valveless micropumps based on SLA and DLP.

Multi-material jetting (MMJ) 3D printing is another type of photopolymerization technology. Instead of using optical scan or projection to selectively solidify pixels to embody digital 3D design, MMJ uses a mobile print head with nozzle arrays, which precisely and rapidly jet droplets of photopolymer resin, to form patterns like paper printers. Immediately after the droplets are deposited onto the build platform, they are cured by an integrated UV light source. The printing inks are separate from each other, making it possible to print multiple colors and materials simultaneously. The overall printing process is similar to printing on large paper and applying different patterns layer by layer, leading to relatively higher production efficiency. MMJ 3D printing exhibits advantageous autonomous multi-material integration and high production efficiency, while maintaining satisfactory resolution and surface properties for pump performance [18,19], suitable for multiple-material components such as check valves and soft membranes. These merits are considered promising for the fabrication of passive-valve electromagnetic micropumps, which show higher rectification efficiency at low frequencies of electromagnetic actuation than valveless counterparts [20]. Taylor et al. applied MMJ to fabricate diaphragm reciprocating vacuum pumps with active pneumatically actuated check valves based on a 3-D printed diaphragm and valve membranes [21]. Their work confirmed the feasibility of MMJ 3-D printing for leak-tight membranes and diaphragms with high operation cycles and vertical resolution. Nevertheless, there has been no previous demonstration of efficient fabrication of cost-effective liquid passive-valve electromagnetic micropumps based on MMJ 3D printing or other additive manufacturing approaches, primarily due to challenges in 3D model design and tailored fabrication techniques. Therefore, verifying the feasibility of MMJ in the efficient fabrication of cost-effective passive-valve electromagnetic micropumps by developing new designs and workflows is critical for enabling integrable electromagnetic micropumps suitable for low-voltage disposable applications and mass production.

This work demonstrates applying MMJ 3D printing in fabricating electromagnetic reciprocating micropumps with ball check valves and a built-in actuation membrane, achieving high-performance micropumps with efficient fabrication and low material cost. A new 3D model design and fabrication workflow for ball-valve reciprocating micropumps are proposed and tested. Experimental optimization of soft-membrane-based micropumps is performed by comparing the performance of prototypes with varying membrane thickness and chamber volume. Fully working micropumps with a small size and good performance are demonstrated. The viscoelastic behavior of the 3D-printed soft membranes during pump operation is characterized. Section 2 introduces details for the design and fabrication of the micropump. Section 3 includes details about the experimental optimization of chamber size and membrane thickness. Section 4 includes the results of flow rate stability tests. In Section 5, a comparison of published electromagnetic reciprocating micropumps and the devices in this work is presented. Section 6 includes a discussion of the limitations of the present study and directions for future work. Section 7 includes conclusions.

2. Device design and fabrication

The schematic diagram explains the general working principle of a ball-valve electromagnetic micropump (Fig. 1a). The micropump comprises a membrane integrated with a magnet, a pump chamber, and two ball check valves. When periodical voltages are applied to the external actuation coil, the vibration of the magnet and the membrane will vary the chamber pressure for pumping. When the membrane is depressed, the outlet check valve is open while the inlet check valve is closed, allowing liquid to flow out. In the next half cycle, the membrane is pulled, the outlet check valve is closed while the inlet check valve is open to suck the liquid into the chamber. These cycles generally happen at frequencies of 1–100 Hz.

The 3D model of the micropump was designed and edited using Autodesk Fusion 360. There are four micropump components in the design, including a membrane component, a chamber component, and two valve housing components (Fig. 1b). The soft parts, which are indicated using blue color, were fabricated using soft 3D printing material (Agilus30 Clear), while rigid parts, which are indicated using gray color were fabricated using rigid material (VeroClear). The four soft parts include one membrane, one chamber sealing on the membrane component, and two check valve seats for sealing, one of which is in the chamber component and the other is in the inlet check valve housing. The diameter of the membrane is 8 mm. The connection between the

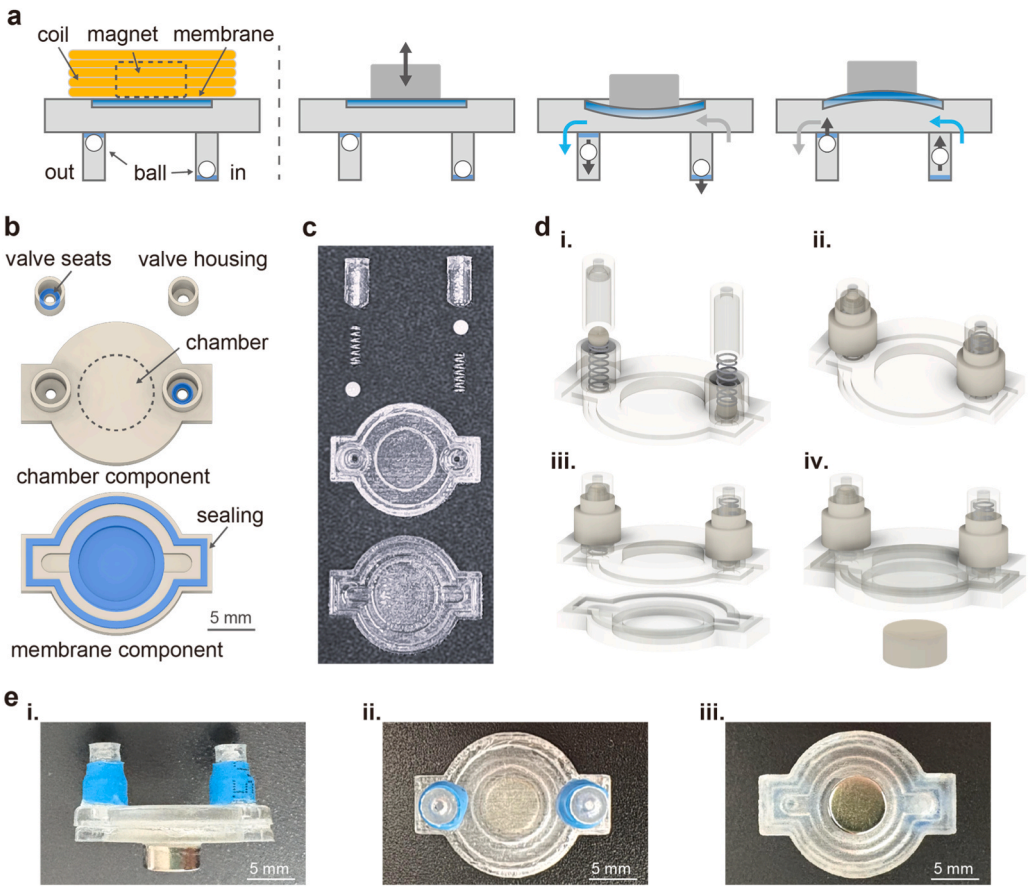


Fig. 1. (a) Schematic diagram for the general working principle of electromagnetic reciprocating micropumps. (b) 3D model design of the device. Blue parts are soft, and gray parts are rigid. (c) Printed components, laid out according to the assembly process. (d) Assembly workflow. (d.i) Place springs, ceramic balls and check valve housings and adjust the height of the check valve housings using a digital vernier caliper. (d.ii) Apply glue to the connection of the valve housings, cover using heat shrink tubes. (d.iii) Chamber part covers the membrane part. (d.iv) Attach the magnet. (e) The physical picture of a micropump prototype. (e.i) Front view. (e.ii) Top view. (e.iii) Bottom view of the micropump.

membrane and the housing is strengthened by adding a ring (Agilus30 Clear) with 8.0 mm inner diameter, 10 mm outer diameter, and 1.0 mm thickness on the membrane component. The height of the soft chamber sealing is 0.50 mm, fitting the groove at the bottom of the chamber component. The check valve sealing seats are designed by cutting the solid cylindrical model with a 1.9 mm diameter ball, fitting the 2.0 mm size of the actual ball parts used in the ball check valve assembly, to reduce leakage in the inlet and backflow in the outlet. To avoid the impact of surface quality during the printing and removal of the Support 705 supporting material, the sealing seats were designed to face upward on the building platform of 3D printing and were printed using a Glossy finish to improve the contact quality and sealing function. The model was then exported as two STL files for rigid and soft parts and imported as an assembly in GrabCAD print software. The GrabCAD advanced slicing was selected in the software to process the STL file into layers. The build mode is Digital Material Mode, with a layer thickness of ~30 μm. The universal print setting was a Glossy finish to improve the surface quality. The temperature of the printing head is ~70 ℃. The value of the head vacuum indicator is ~6. The calibrated right-side UV light source is on to cure the polymer ink jetted from the printer head. The printing time for one batch of 20 devices is approximately 45 min (combination of the check valve housing, chamber components, and membrane components). After printing, the supporting material on the components was removed manually and cleaned using flowing water. Cleaned components, springs, and ceramic balls for check valves are presented in Fig. 1c.

Characterizations have been conducted to estimate the printing quality and material properties. The horizontal and vertical dimension characterizations using a microscope indicate the overall consistency of dimensions between design and the actual 3D printed parts (Figure S1-3). The accuracy is limited but acceptable for all thin-walled vertical annuli with sub-millimeter wall thickness, including the height of vertical annuli the check valve housing (Figure S1c and Figure S2c) and the height of vertical annuli in the chamber component (Figure S3e), and the wall thickness of the soft sealing parts (Figure S2a and Figure S3d). The surface roughness was tested using AFM and an optical profiler to measure both small-area and large-area surface quality of the printed components. The tested surfaces include the bottom and upper surfaces of the chamber component, and the upper surface of the soft membrane (upper means it contacts with air; bottom means it contacts with the supporting material), abbreviated as bottom chamber, upper chamber, and soft membrane. Particularly, the samples for optical profiler characterization were coated with a thin layer of Au of several nanometers, which enhances reflection and is considered negligible for the large area surface roughness of several micrometers. The average square-root roughness Rq of AFM tests is 102 nm, 39 nm, and 121 nm and Rq from optical profiler tests is 4.1 μm, 2.8 μm, and 4.6 μm for the bottom chamber, upper chamber, and soft membrane, respectively (Figure S4). The surface of the upper chamber is smoother than that of the other surfaces. Small holes could be relevant to gas escape during 3D printing (Figure S4b). Obvious striped defects can be observed (Figure S4 d-f), especially in the bottom chamber sample due to the supporting material (Figure S5). The roughness of the soft material is intrinsically higher in both small and large areas, though it doesn't contact the supporting

material. Inter-material adhesion was qualitatively tested by using the tweezers' tip to tear the soft material from the rigid material (see video S1). The result indicates good inter-material adhesion in MMJ 3D-printed components in this work. The mechanical property of the printed soft material was tested in bulk cylinder samples with an 8-mm diameter and 2-mm and 3-mm thickness using a dynamic mechanical analyzer. The consistent measurement results indicate a storage modulus of 0.9–1.1 MPa, close to conventional rubber materials. The material also shows a strong viscoelastic property, with a loss modulus of 0.5–0.6 MPa (Figure S6).

A simple assembly workflow taking less than 5 min is desired (Fig. 1d). First, stainless-steel compression springs and ceramic balls were placed inside the cylindrical holes on the chamber component according to the flow direction, i.e. the ceramic ball is on top of the spring for the inlet and is below the spring for the outlet. In this way, the ceramic ball presses on the valve seat on the tubing connection side in the inlet check valve; for the outlet valve, the ball interfaces to the sealing seat on the chamber component. Then the valve housing parts were inserted into the hole to cover the springs and balls. A digital vernier caliper was used to clamp the membrane and valve housing parts to efficiently adjust the inlet and outlet valves to the target length as the valve housing moves with the adjustment of the vernier caliper (Fig. 1d.i). Subsequently, glue was applied to the connection of valve housings and then heat shrink tubes for connection strengthening were applied around the valve housing and then dried using hot air within seconds (Fig. 1d.ii). Then the membrane and chamber parts were bonded using glue by applying glue on the outer periphery of the chamber sealing (Fig. 1d.iii). Later, a 6 × 3 mm N52 NdFeB permanent magnet was attached to the center of the membrane with glue (Fig. 1d.iv). The full device size is 20 × 15 × 13 mm^3 and 20 × 15 × 10 mm^3 excluding tube connection parts. (Fig. 1e). These device dimensions have been used for all the following optimization and stability experiments.

3. Device optimization

3.1. Optimization indicators and device characterization

The indicators for optimization include backpressure at zero flow rate and flow rate at zero backpressure. The former reflects the output fluidic resistance tolerance and the latter reflects the compatibility with various applications. In addition, these two parameters indicate pump operation efficiency. During device characterization, the micropump was held by a bench vice, with the side of the permanent magnet facing upward. An air-core coil was pressed on the flat surface of the membrane component to keep the magnetic actuation distance and the permanent magnet in the center. The outlet and inlet of the micropump were connected to the output and input reservoir through polyvinyl chloride (PVC) tubing (Fig. 2a). For flow rate measurement, a digital balance was placed under the output reservoir to measure and read out the real-time liquid mass in the output reservoir (Fig. 2bi). The flow rate is recorded at an interval of about 1.45 s per reading. The flow rate of water was calculated by applying linear fitting to the weight increment curves. For backpressure, the hydrostatic pressure of a water column between the outlet of the PVC tubing and the pump outlet was changed by adjusting the height difference between the pump outlet and the tube outlet (Fig. 2bii). The height difference for zero flow rate was recorded [22].

3.2. Chamber size selection

In previous work [23,24], researchers developed numerical simulation models for valveless micropumps to evaluate and optimize the pump design. Such models are useful for basic functionality predictions or to investigate the effect of specific design and fabrication details. However, the overall device performance is challenging to predict because more complex fabrication and operational details are difficult to simulate. In addition, the operation of mechanical check valves is challenging to predict by dynamic finite element modeling at the accuracy required for device design optimization. Benefiting from rapid prototyping of 3D printing, in this work, direct experimental optimization of soft-membrane-based micropumps was conducted by fabricating and testing a series of prototypes with variable design characteristics.

In a first experiment, a modular device with various chamber volumes was designed and fabricated. The design of check valves was kept constant in this device series to avoid interference from check valve fabrication. The check valve heights (Figure S7) for the inlet and outlet are approximately 6.5 mm and 6.7 mm, respectively. The membrane thickness for this experiment is 300 μm. As shown in Fig. 3a, the vertical chamber depth is comprised of three parts, namely the adjustable chamber depth x (in the chamber component), liquid channel (0.5 mm, in the membrane component), and default chamber depth (0.7 mm, in the membrane component). In this experiment, the chamber size was varied by adjusting the chamber depth in the chamber component using 3D-printed filling discs of various thicknesses. The initial depth of the adjustable chamber is 1.50 mm. The thicknesses of the 3D printed discs (VeroClear) are 0.50 mm, 0.75 mm, 1.00 mm, 1.25 mm, and 1.50 mm (Fig. 3b). Hence, the remaining adjustable chamber depths are 1.00 mm, 0.75 mm, 0.50 mm, 0.25 mm, and 0 mm, respectively. The remaining depth was confirmed using a digital vernier caliper after placing the disc and was rechecked before changing the disc to the next size, confirming the reliability of surface tension for binding the disc on the chamber part. When changing the chamber size, the membrane component needs to be separated from the micropump manually using tweezers. The groove for the sealing parts is then cleaned thoroughly. After replacing the disc, a new membrane component is glued, with all other components remaining the same.

The flow rate and backpressure versus frequency for different adjustable chamber depths were measured (Fig. 3c and d). The original 1.50 mm device shows a flow rate and backpressure of zero and is excluded from the figure. Both the maximum flow rate and backpressure are achieved by the 0.50 mm prototype (Fig. 3e and f). The results indicate that the micropumps work better in terms of flow rate and backpressure for intermediate chamber sizes. The performance

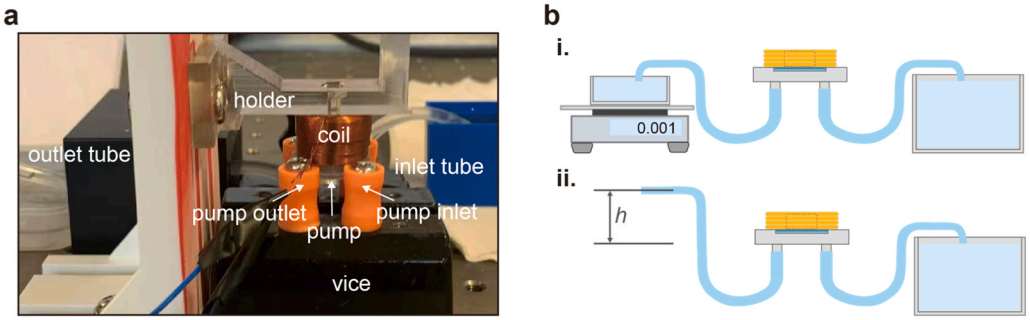


Fig. 2. (a) Device characterization system. (b) Schematic diagram for measurement setups. (b.i) Flow rate measurement. (b.ii) Backpressure measurement.

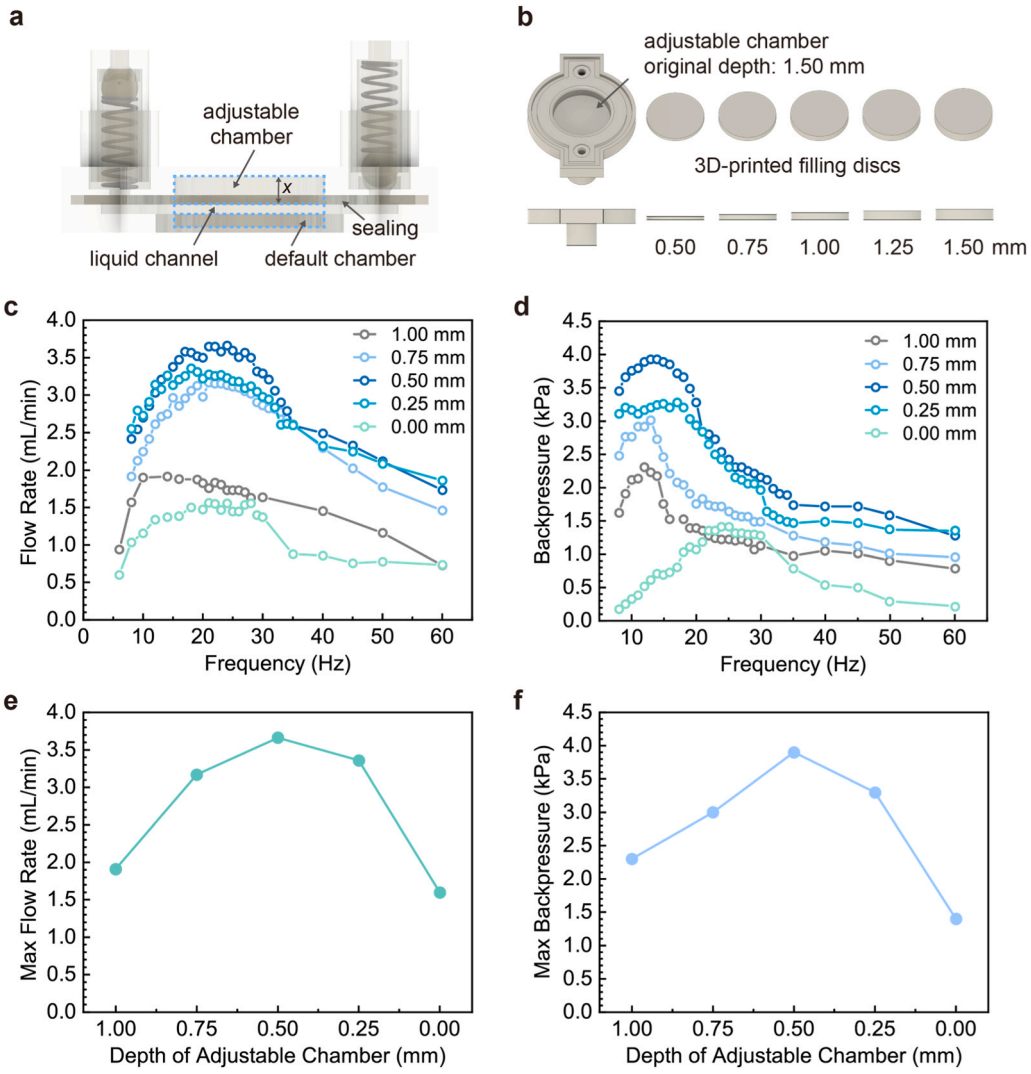


Fig. 3. (a) Schematic diagram for the composition of chamber depth. (b) Schematic diagram for the method of chamber depth adjustment based on 3D-printed filling discs. (c) Pump flow rate versus the frequency of excitation current. (d) Backpressure versus the frequency of excitation current. (e) Maximum flow rates of different chamber sizes (f) Maximum backpressure of different chamber sizes.

limitation of small chambers is attributed to local liquid response, such as local compression, vibration, and friction, that consumes activation energy for pushing out liquid. The reduced performance of large chambers is attributed to larger fluidic inertial effects and fluidic impedance, resulting in lower output for the same activation driving force. Similar trends were reported in the literature; they were attributed to flow losses due to small flow cross-sectional areas for small chamber volume and losses of activation energy due to liquid damping for large chamber volume [23,24]. These results demonstrate that the experimental parametric optimization method adopted, based on rapid MMJ prototyping, offers fast and reliable identification of the preferred pump chamber volume for a given device scale.

3.3. Membrane thickness selection

Another important pump design parameter is the thickness of the membrane, which determines stiffness and thereby vibration amplitude for a given excitation. In turn, this influences the stroke volume and the driving pressure [24]. To investigate this effect, devices with membranes of 100 μm, 300 μm, and 650 μm were evaluated. The actual fabricated thicknesses were confirmed by printing the three membranes on the same substrate (Figure S8) and measuring their thickness with respect to the substrate by a high-resolution optical profilometer based on a laser displacement sensor and a linear translation stage. An optical measurement method was preferred over mechanical scanning because of the high softness of the material used. To enhance reflection, the as-printed clear material was spray-colored for this measurement. The corresponding thicknesses were measured to be 661 ± 7 μm, 323 ± 3 μm, and 104 ± 4 μm, respectively, demonstrating a fabrication deviation from the design value below 10 % (Fig. 4a). All other pump design parameters were kept the same. The check valve heights for the inlet and outlet were 6.5 mm and 6.7 mm, respectively. The workflow for changing the membrane component is identical to the workflow introduced in Section 3.2 for the chamber size selection experiment.

As shown in Fig. 4b, the flow rate increases as the membrane thickness decreases. The frequency scan curves comply with the fitting curve (R^2 values are 0.85, 0.90, and 0.76 for the 100-μm, 300-μm, and 650-μm devices, respectively) using the model based on the RLC equivalent circuit [7,25,26], meaning the flow rate change versus frequency is mainly caused by stroke cycle numbers with constant stroke volumes and system fluidic impedance, rather than the resonant vibration of membranes. This is supported by the vibration amplitude versus frequency of excitation current (Figure S9). Maximum flow rates are 6.9, 3.9, and 0.4 mL/min, respectively, for an actuation power of 1 W (Fig. 4b). The maximum backpressures are 3.0, 1.4 (3.9 kPa in a 300-μm device in Section 3.2), and 0.6 kPa for an actuation power of 1 W

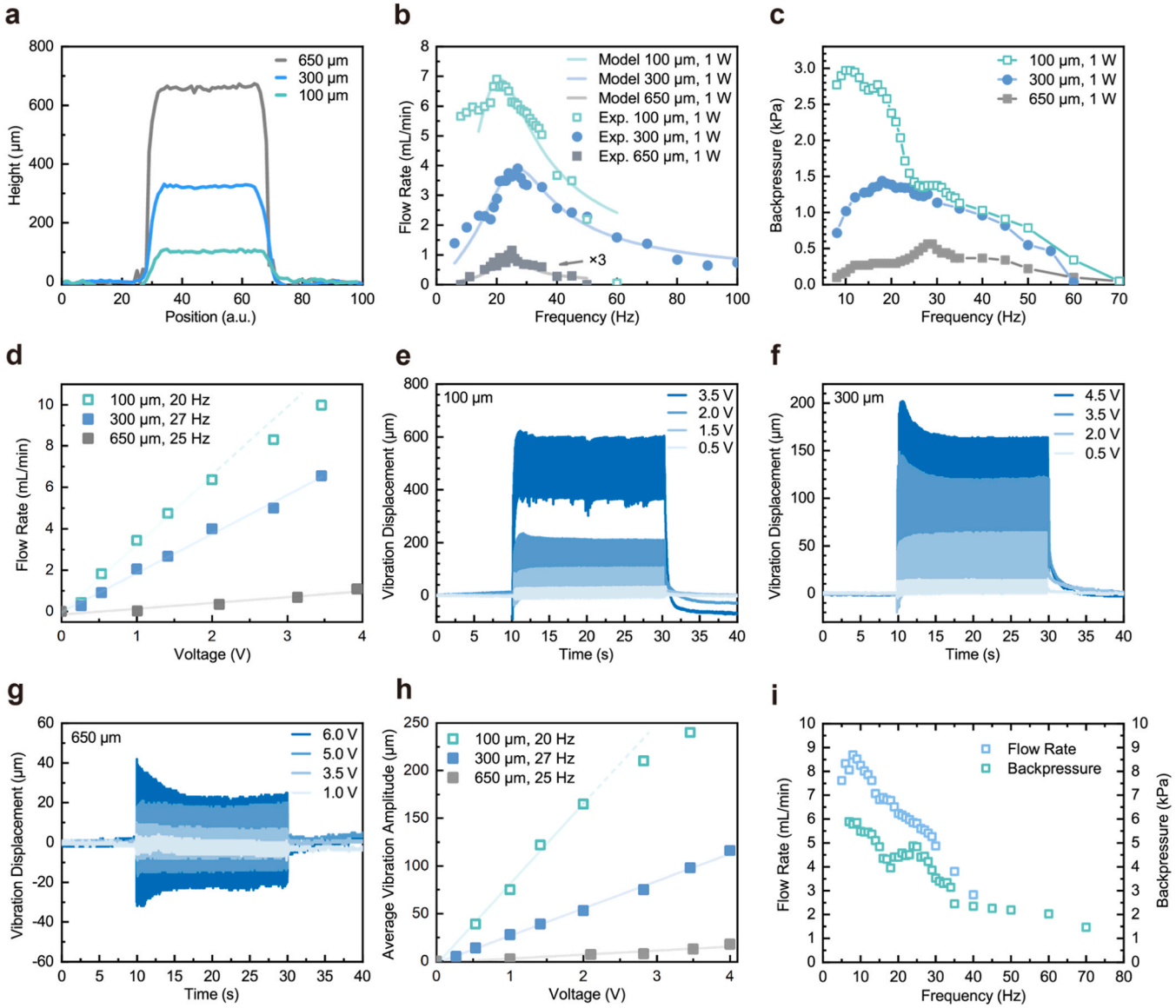


Fig. 4. (a) Height measurement of three membranes on the same substrate. (b) Pump flow rate versus the frequency of excitation current. Solid lines are fitted curves using the fluidic RLC model. (c) Backpressure versus the frequency of excitation current. (d) Comparison of pump flow rate versus excitation voltage. Solid lines are linear fits. (e) Vibration displacement curves for various voltages for a 100-μm device. (f) Vibration displacement curves for various voltages for a 300-μm device. (g) Vibration displacement curves for various voltages for a 650-μm device. (h) Comparison of average peak-to-peak vibration amplitude of the membranes versus excitation voltage under pump operation. Solid lines are linear fits. (i) Flow rate and backpressure versus frequency of the best 100-μm device. The actuation power is 1 W.

(Fig. 4c), indicating inefficient power transfer from the actuation magnetic field to thick membrane vibration. Similar to the frequency scan of flow rate, the flow rate versus voltage also shows substantial enhancement as the membrane thickness decreases (Fig. 4d), indicating the significant increase in stroke volume at the same level of actuation magnetic field. In addition, deviation from the linear increase trend owing to stretch limitation is observed in 100-μm device. The R^2 values for the fits are 0.99, 0.99, and 0.90 for the 100-μm, 300-μm, and 650-μm devices, respectively.

To directly access the actual vibration amplitude of the membrane vibration, a laser displacement sensor was applied during pump operation, with the laser spot on the magnet. The micropump was actuated using the same coil energized by sinusoidal current (Figure S10). At 10 s, the power supply was turned on, and the pump started to work. At 30 s, the power supply was turned off. The membrane vibration measurement is overall robust in multiple measurements, showing almost same vibration displacement curves, though the equilibrium position may change for 100-μm device because of large deformation and low stiffness (Figure S11). As shown in the results of the vibration profiles under different voltages, there are differences in the initialization region, vibration equilibrium position, and vibration amplitude under varying force inputs (Fig. 4e-g). The profiles comply with the superposition of material viscoelastic characteristics such as creep, recovery [27,28], and actuation signal characteristics of sinusoidal vibration (Figure S12a and c, Figure S13a and c, and Figure S14a and c). The vibration frequency is consistent with the excitation frequency according to the cycle number in one second of the zoomed-in figures (Figure S12b and d, Figure S13b and d, and Figure S14b and d). These results indicate a transition to steady vibration within 5 s after actuation. On the other hand, a positive steady-state deformation was formed as the equilibrium position. It is an acceptable feature and a reasonable physical phenomenon. For the push half-cycle, the magnetic force on the membrane overcomes the chamber pressure and the membrane spring force; for the suction half-cycle, the magnetic force overcomes the negative pressure in the chamber and the

membrane spring force to lift the membrane. In the working prototypes, the chamber pressure in the push cycle is larger than the chamber negative pressure generated during the membrane upward movement due to the large dead volume. Thus, it results in a larger net force toward the upward direction and a positive steady-state deformation. The actual average peak-to-peak vibration amplitude at different voltages for 100-μm, 300-μm, and 650-μm membranes was analyzed. The results show a linear relationship of vibration amplitude versus voltage (Fig. 4h). The R^2 values for the fits are 0.99, 0.99, and 0.91 for the 100-μm, 300-μm, and 650-μm devices, respectively. Similar to Fig. 4d, deviation from the linear increase trend owing to stretch limitation is observed in the 100-μm device. These results indicate that the reduction in membrane thickness contributes to larger vibration amplitude and thereby larger stroke volume under the same excitation condition, leading to performance enhancement in backpressure, flow rate, and efficiency. The fragility and durability of thinner membranes limit a minimum of 100 μm. The maximum flow rate and backpressure for 100-μm micropumps are 8.7 mL/min and 5.9 kPa at 1 W excitation power (Fig. 4i). Larger peak-to-peak vibration amplitude for the 100-μm soft membrane at lower frequencies was observed (Figure S15a). This is attributed to a more complete strain response due to smaller viscoelastic damping (delayed response) at lower frequency, meaning the membrane has enough time to deform thoroughly when the frequency is low. Larger strokes stemming from large vibration amplitude increase the total liquid output (Figure S15b), as the flow rate is nearly proportional to the product of frequency and stroke per cycle at low frequencies [7, 26].

4. Flow rate stability

Apart from flow rate and backpressure, flow rate stability is another important dimension for assessing reliability, especially for applications requiring long-term, precise fluidic control. The flow rate stability of the micropump was characterized when the pump was working under different flow rates. Different from the average flow rate from the fitting of weight increment curves over a period, the flow rates here are instant flow rates calculated using (weight2-weight1)/(t2-t1). The digital balance takes one data string per 1.45 s, with the instant flow rate being the average flow rate for a 1.45-second interval.

The flow rates of a 100-μm prototype for levels of 1–2, 2–3, 3–4, 4–5, 5–6, 6–7, 7–8 mL/min were measured continuously for 150 s. Fig. 5a includes three discrete curves with a certain level of absolute fluctuation. Statistical analysis confirmed the standard deviation of flow rates is within the range of 0.4–0.7 mL/min (Fig. 5b), which is attributed to the operation of check valves and fluctuating pump strokes. The coefficient of variation (CV) value decreases with the increase in the flow rate because of the small change in the standard deviation (numerator) and the large change in the mean (denominator) for CV calculation (Fig. 5c). For flow rates from 4 to 7 mL/min, the CV values as low as 6–11 % compare well with other micropumps with high flow rate stability [29, 30], indicating good flow rate stability and feasibility for certain practical applications. The results of the 300-μm prototype show a similar trend, while the CV value cannot go below 10 % due to the limitation of the max flow rate of ~4 mL/min (Figure S16).

The causes of the observed flow rate stability (0.4–0.7 mL/min of standard deviation) may primarily stem from the instability of membrane vibration and check valves. On the one hand, the magnet may press and drag the membrane in inefficient vibration modes, such as swing vibration. On the other hand, the check valves are not robust enough, resulting in unstable rectification performance. For reducing standard deviation, potential strategies include constraining the vibration mode to vertical movement and improving check valve robustness.

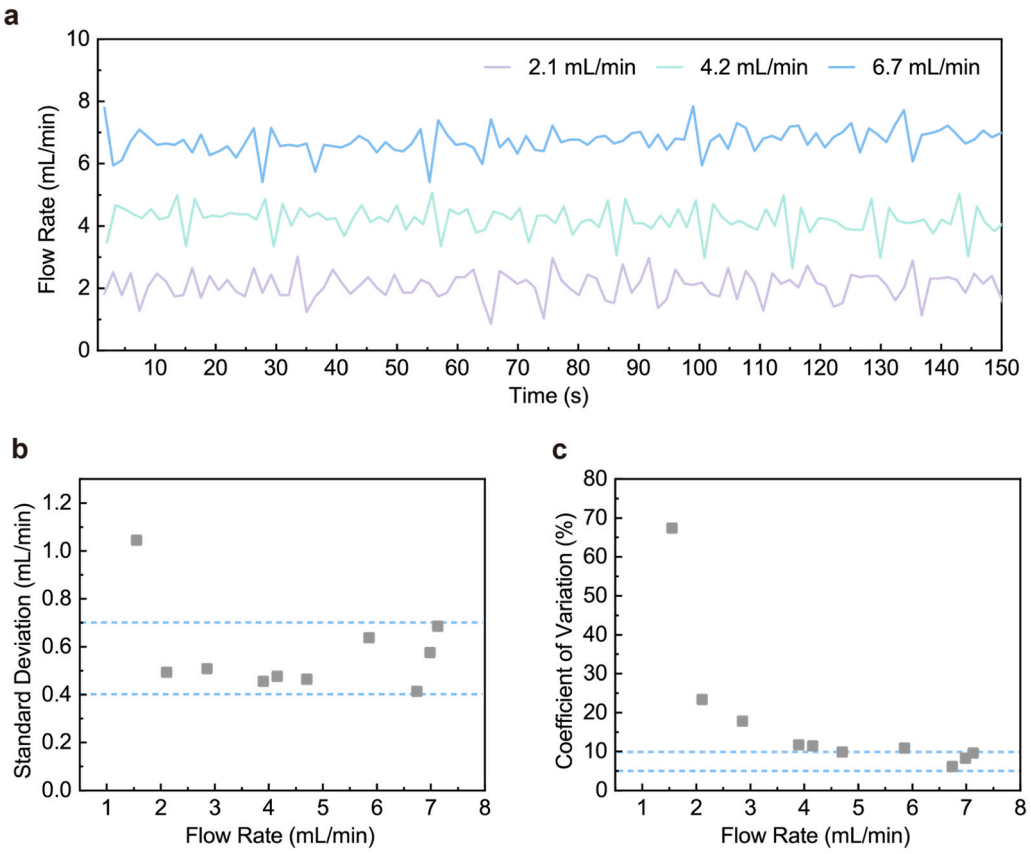


Fig. 5. (a) Curves of instant flow rate of a 100-μm prototype for three flow rate levels. (b) Standard deviation of flow rates of a 100-μm prototype at different flow rates. (c) Coefficient of variation of flow rates of a 100-μm prototype at different flow rates.

5. Comparison of single-coil electromagnetic reciprocating micropumps

Table 1 summarizes single-coil electromagnetic reciprocating micropumps, focusing on key characteristics, such as fabrication methods, valve types, flow rate, backpressure, power efficiency, and device size. The prototype size in this work is similar to or smaller than its counterparts. The device performance in this work is better than all its counterparts based on other valve types and fabrication techniques, such as molding, sheet stacking, and FDM 3D printing, except for the backpressure of one PDMS prototype [6] and one prototype actuated by a special iron-core coil [7]. It is noted that actuation methods influence the performance of micropumps. Coils with an iron core and specially designed magnetic fields can significantly improve membrane vibration owing to the large magnetic force [7]. Other alternative actuation methods, such as motor-based rotational magnets, often show higher efficiency [6,11]. A standardized driving approach will benefit cross-study comparisons but is still challenging in the community. The efficiency and the flow rate range of ball valves are significantly higher and broader than for the diffuser-nozzle type, primarily due to unsatisfactory rectification performance of diffuser-nozzle structures from both design and fabrication accuracy, and negative effects such as flow fluctuation at low-frequency magnetic actuation [17].

In addition to good performance, this work also shows lower fabrication complexity and cost. For the 3D printing process, components for 20 micropumps could be automatically printed in 45 min. The manual assembly process usually takes less than 5 min. Given the average power consumption of the 3D printer as 2 kW, the printing power consumption is estimated to 0.08 kWh per micropump. The consumption of Agilus30Clear is 4 g, VeroBlackPlus used in support is 4 g, Veroclear is 17 g, and FullCure705 is 16 g; The reference retail price with value-added tax for Agilus30Clear is 0.23 £ /g, VeroBlackPlus is 0.19 £ /g, Veroclear is 0.29 £ /g, and FullCure705 is 0.11 £ /g. Thus, the total 3D printing material cost for 20 devices is approximately 8.4 £ . Considering the costs of ceramic balls, magnets, and springs for each device of approximately 0.1 £ , 0.1 £ , and 0.5 £ , respectively, the material cost for each current prototype is ~1.1 £ . Costs of equipment, labor, and post-processing are not considered in this estimation due to complexity. The material cost could be further reduced by decreasing the thickness of the components and choosing cheaper alternative suppliers for magnets, ceramic balls, and springs.

6. Discussion

6.1. Power efficiency and energy loss

Possible energy loss channels include Joule heat in the actuation coil, ineffective vibration in magnet movement, viscoelastic loss, and fluidic resistance loss. Regarding the actuation source, the resistance and inductance of the coil are ~3.9 Ω and 1.6 mH. At the low frequencies used (below 100 Hz), the total impedance is around 4 Ω. The heat generation power for a 2 V RMS voltage is ~1 W. Thus, most of the energy in the actuation coil is actually dissipated in the form of Joule heat. The magnetic coupling is high as the magnet is actually inside the coil and accepting almost all the magnetic flux. However, the magnet might not be perfectly oriented, causing non-vertical vibration, which doesn't efficiently induce volume change for pumping and causes abnormal deformation of the membrane. Besides, unbalanced vibration also influences the rectification of check valves. Viscoelastic loss is another issue. The loss modulus is ~ 0.5 MPa for the printed membrane material, meaning the kinetic energy of the magnet will be partly converted to heat generation in the soft member due to the movement of polymer chains. Furthermore, fluidic resistance and fluidic damping also cause energy loss before the liquid is finally pushed out. Potential improvement strategies include reducing the resistance of the coil, constraining the movement of the magnet in efficient modes, reducing viscoelastic loss and fluidic resistance.

6.2. Long-term operation stability

The current operational stability T_{50} (time for flow rates to decay to half of the original values) is around tens of minutes to several hours, by monitoring the flow rate decay of fresh devices (Figure S17). The current devices suffer from abrupt changes in flow rate (Figure S17a), which is attributed to unstable rectification of check valves. This may stem from the failure of sealing parts, or the position change of the springs and ceramic balls. In addition, the slow decay (Figure S17b) is attributed to membrane aging, which may be caused by membrane fatigue and water absorption (swelling). This could be more obvious in the low flow rate range due to insufficient driving force to overcome membrane damping. However, a promising indication is the observation of signs of stable operation, such as the first 11 min and 17–25 min of Figure S17a, which shows almost negligible decay. The results indicate potential stable devices driven at high flow rate with robust check valve rectification.

Table 1
Comparison of single-coil electromagnetic reciprocating micropumps. † indicates that the value is estimated by the present authors according to the original description in the paper.

reference	fabrication	valve type	actuation	flow rate (mL/min)	backpressure (kPa)	power (W)	efficiency	size (mm^3)
[6]	PDMS molding, PDMS film	ball	air core coil	1	3.6	0.5	3×10^{-3}%†	15 × 10 × 5†
[7]	PMMA sheets, PDMS film	ball	iron core coil	3.6	20	0.5	6×10^{-2}%	36 × 18 × 14.5†
[8]	PDMS molding, PDMS film	diffuser	air core coil	4.5×10^{-3}	N/A	8 V	N/A	40 × 20 ×N/A†
[22]	PMMA sheets, PDMS film	diffuser	soft iron core coil	0.40	1.2	150 mA	N/A	36 × 22 × 3
[24]	PDMS molding, PDMS film	diffuser	soft iron core coil	0.051	0.35	0.7†	1×10^{-5}%†	20 × 10 ×N/A†
[31]	PDMS molding, PDMS film	diffuser	soft iron core coil	1.2×10^{-3}	N/A	0.7	N/A	20 × 20 × 2
[32]	PDMS molding, PDMS film	diffuser	soft iron core coil	0.32	0.95	1.3†	1×10^{-5}%†	20 × 12 × 3.5
[9]	3D printing (FDM)	diffuser	air core coil	2.4×10^{-3}	N/A	N/A	N/A	18 × 18 × 5†
[10]	3D printing (FFF)	ball	iron core coil	1.37	N/A	24 V	N/A	21 × 21 × 23†
300 μm, this work	3D printing (MMJ)	ball+spring	air core coil	3.7	3.9	1	6×10^{-3}%	20 × 15 × 10
100 μm, this work	3D printing (MMJ)	ball+spring	air core coil	8.7	5.9	1	2×10^{-2}%	20 × 15 × 10

Improvement strategies include mixing rigid material for the membrane, coating for chemical resistance, and improving check valve design and fabrication.

6.3. Reproducibility and batch-to-batch consistency

To assess the reproducibility and batch-to-batch consistency, the distribution of maximum flow rate across the 40 devices fabricated using components from 2 batches is used as an indicator. The mean max flow rates are 5.5 and 5.4 mL/min, and the standard deviation values are 1.7 and 1.8 mL/min for batch 1 and batch 2 (Figure S18). The results indicate a certain level of batch-to-batch consistency regarding the mean maximum flow rate and the standard deviation. However, the distribution shapes are different for each batch, possibly because of insufficient statistical sample size or batch-to-batch consistency. The major problem is the performance distribution in each batch. The relative standard deviation values are high, with values around 30 %. The underlying reasons for the inconsistency may be the current process for integrating magnet and membrane (position accuracy, glue overflow), unwanted vibration modes due to magnet orientation, and the robustness of the check valves. The implementation of machine automation could be helpful for better performance consistency.

6.4. Workflow scalability

The workflow scalability can be divided into 3D printing and assembly. For 3D printing workflow scalability, the maximum capacity for the Objet500 Connex3 was estimated. For each batch, the maximum capacity for the check valve housing is at least 1500 units per batch, considering the sparse arrangement (Figure S19a). The batch time consumption is ~6 h due to the height. The maximum capacity for chamber and membrane components is ~190 units per batch (Figure S19b), costing 3.2 h for each batch. Thus, components for 1500 devices could be printed in 32 h, including one batch of check valve housing and 8 batches of chamber and membrane components. This estimation indicates the high yield and potential scalability for component manufacturing using MMJ 3D printing. The time consumption could be further reduced by decreasing the height of the components. For higher production yield, an alternative is using MMJ 3D printing mainly for membrane components and the check-valve sealing parts, and using injection molding for other plastic structural parts.

The current assembly workflow involves manual assembly, and this has caused issues in reproducibility and batch-to-batch consistency. A potential solution is presented in a flow chart (Figure S20), where manual steps are needed primarily for placing pre-combined ball/spring modules and the check-valve housing. With the help of commercially available automated dispensing and pressing machines commonly used in the fabrication of electronic devices, workflow scalability is possible. A workflow with such automation will increase assembly efficiency as well as improve the repeatability and accuracy of check valve heights, and consistency of magnet/membrane integration.

6.5. Fluids with different properties

For different types of liquids (viscosity, composition, etc.), compatibility in terms of propulsion capability and chemical resistance is necessary for micropumps to fit various applications. The flow rate of pumping sunflower oil (viscosity of 61 mPa·s) and montmorillonite powder suspension (3.6 g powder in 100 g water) is presented in Figure S21 to evaluate the compatibility with liquids of different viscosities and complexity. At 1 W actuation power, the flow rate of sunflower oil is 1–2 mL/min, and powder suspension is 5.3 g/min, indicating acceptable performance in pumping suspensions and liquids with a wide viscosity range. More types of liquids should be tested, such as blood and cell suspensions. Surface coating is necessary for better chemical resistance for broader types of liquids.

6.6. Potential directions for future work

Besides the above outlook for power efficiency, flow rate stability, operational stability, reproducibility, batch-to-batch consistency, and fluid type compatibility, it would also be important to explore more specific application scenarios of current micropumps to increase demand. Assembly-free (monolithic) design and workflow using MMJ or other 3D printing techniques is welcome in this field for reducing manual steps and improving reproducibility.

MMJ printing is good at the integration of soft and rigid materials, so it is a good candidate for pumps with active soft valves, which has been demonstrated [21]. In that work, the rubber-like valve membranes have not leaked after over 2 million cycles. Another possibility is the peristaltic type, which requires periodic and alternate pressing and releasing of soft material. It is possible to integrate multiple soft membranes and chambers. The actuation force can alternately press the soft membrane to realize peristaltic liquid propulsion [14]. The main limitations are chemical stability, as well as the tradeoff between the durability and the stiffness of soft membranes. Surface coating or material development is necessary for better chemical stability. Better material choices for high-toughness, high-fatigue-resistance soft membranes are crucial for applications requiring long-term periodic large deformation.

7. Conclusions

In conclusion, this work successfully demonstrated the proposed 3D model and fabrication technique based on MMJ 3D printing, enabling the efficient fabrication of cost-effective electromagnetic micropumps using automated 3D printing and a simple assembly workflow. The full device size is $20 \times 15 \times 13$ mm^3 and $20 \times 15 \times 10$ mm^3 excluding tube connection parts. Experimental optimization of soft-membrane-based micropumps is performed by comparing the performance of prototypes with varying chamber volume and membrane thickness. The adjustable chamber depth and the membrane thickness of the best device are 0.50 mm and 100 μm. The flow rate and backpressure deteriorate for smaller and larger chamber sizes. The flow rate increases as the membrane thickness decreases. Wirelessly actuated by an air-core coil, the maximum flow rate and backpressure of 8.7 mL/min and 5.9 kPa at 1 W correspond to an efficiency of 2×10^{-2}%. The membrane shows viscoelastic behavior during pump operation. The flow rate improvement was attributed to a larger vibration amplitude stemming from the lower stiffness of the thinner membrane. Flow rate stability tests show the coefficient of variation down to 6–11 % for an instant flow rate range of 4–7 mL/min for 100-μm devices, confirming the potential for practical applications. The performance, including flow rate, backpressure, power efficiency, and flow rate stability, compares well with the counterpart micropumps. Besides efficient fabrication and good performance, this work also shows the advantage of low material cost, which is ~1.1 £ per device in material and 0.08 kWh in energy consumption at prototype volumes. Therefore, this work proves the feasibility of MMJ 3D printing for liquid micropumps using the proposed new 3D model design and tailored fabrication workflow and shows the great promise of MMJ 3D printing for cost-effective miniature micropumps suitable for mass production and low-voltage disposable applications.

8. Experimental section

8.1. Materials and equipment

Air core coil (length: 1.2 cm, inner diameter: 0.8 cm, outer diameter: 1.9 cm, resistance 3.9 Ω, inductance: 1.6 mH, Gikfun). Shrink tubes (diameter: 5 mm, length: 3.9 mm, Eventronic). Zirconium Oxide G10 ceramic bearing ball: 2 mm. Permanent Neodymium magnet: N52 6 mm× 3 mm. Spring: CIM020AA 02S, LEE SPRING. Glue: Loctite Precision. Tubes: PVC Clear Vinyl Tubing inner diameter: 3 mm, outer diameter: 5 mm, sourcing map.

Digital Vernier Caliper: 150 mm, Kynup. Digital balance: Gram FC 200, Gram Lite. Optical profilometer: LK-Navigator 2 (LK-G5000), KEYENCE. 3D printer: Objet500 Connex3, Stratasys. Microscope: VHX-2000 microscope, Keyence. Optical Profiler: Detack 3ST Surface Profiler, Veeco. Dynamic Mechanical Analyzer: RSA-G2 Solids Analyzer, TA Instruments. Atomic Force Microscope: Asylum MFP-3D classic, Oxford Instruments. Rheometer: HR20, TA Instruments.

CRediT authorship contribution statement

Michail E. Kiziroglou: Writing – review & editing, Writing – original draft, Supervision, Resources, Project administration, Methodology, Investigation, Funding acquisition, Formal analysis, Data curation, Conceptualization. **Xiaotong Guo:** Writing – review & editing, Resources, Methodology. **Eric M. Yeatman:** Writing – review & editing, Writing – original draft, Supervision, Resources, Project administration, Methodology, Investigation, Funding acquisition, Formal analysis, Data curation, Conceptualization. **Xu Chen:** Writing – review & editing, Resources, Methodology. **Chen Lin:** Writing – review & editing, Writing – original draft, Visualization, Validation, Software, Resources, Project administration, Methodology, Investigation, Funding acquisition, Formal analysis, Data curation, Conceptualization. **Zeyu Wang:** Writing – review & editing, Resources, Methodology.

Declaration of Competing Interest

The authors declare that they have no known competing financial interests or personal relationships that could have appeared to influence the work reported in this paper.

Acknowledgments

The authors gratefully acknowledge the financial support from the Imperial College President's PhD Scholarship (to C. Lin). The authors acknowledge Fabio Tatti for providing the reference retail price for 3D printing materials and technical support for 3D Printing. The authors acknowledge Qindong Zheng for support with the microscope. The authors acknowledge Wenkun He for support with the optical profiler. The authors acknowledge Andrew Erwin for support with the dynamic mechanical analyzer. The authors acknowledge Peter K. Petrov and Zelong Yan for support with the Atomic Force Microscope. The authors acknowledge William Megone for support with the rheometer.

Appendix A. Supporting information

Supplementary data associated with this article can be found in the online version at doi:10.1016/j.addma.2025.105038.

Data availability

Data will be made available on request.

References

[1] D.J. Laser, J.G. Santiago, A review of micropumps, J. Micromech. Micro 14 (6) (2004) R35–R64, https://doi.org/10.1088/0960-1317/14/6/r01.
[2] X. Luo, L. Yang, Y. Cui, Micropumps: mechanisms, fabrication, and biomedical applications, Sens. Actuators A Phys. 363 (2023) 114732, https://doi.org/10.1016/j.sna.2023.114732.
[3] D. Maillefer, S. Gamper, B. Frehner, P. Balmer, H. van Lintel, P. Renaud, A high-performance silicon micropump for disposable drug delivery systems, Tech. Dig. MEMS 2001 Conf. Interlake (2001) 413–417, https://doi.org/10.1109/memsys.2001.906566.
[4] P. Woias, Micropumps—past, progress and future prospects, Sens. Actuators B Chem. 105 (1) (2005) 28–38, https://doi.org/10.1016/s0925-4005(04)00108-x.
[5] S. Mohith, P.N. Karanth, S.M. Kulkarni, Recent trends in mechanical micropumps and their applications: a review, Mechatronics 60 (2019) 34–55, https://doi.org/10.1016/j.mechatronics.2019.04.009.
[6] T. Pan, S.J. McDonald, E.M. Kai, B. Ziaie, A magnetically driven PDMS micropump with ball check-valves, J. Micromech. Micro 15 (5) (2005) 1021–1026, https://doi.org/10.1088/0960-1317/15/5/018.
[7] M. Shen, C. Yamahata, M.A.M. Gijs, A high-performance compact electromagnetic actuator for a PMMA ball-valve micropump, J. Micromech. Micro 18 (2008) 025031, https://doi.org/10.1088/0960-1317/18/2/025031.
[8] S. Mi, H. Pu, S. Xia, W. Sun, A minimized valveless electromagnetic micropump for microfluidic actuation on organ chips, Sens. Actuators A Phys. 301 (2020) 111704, https://doi.org/10.1016/j.sna.2019.111704.
[9] D.J. Thomas, Z. Tehrani, B. Redfearn, 3-D printed composite microfluidic pump for wearable biomedical applications, Addit. Manuf. 9 (2016) 30–38, https://doi.org/10.1016/j.addma.2015.12.004.
[10] A.P. Taylor, L.F. Velásquez–García, Low-cost, monolithically 3D-printed, miniature high-flow rate liquid pump, J. Phys. Conf. Ser. 1407 (2019) 012040.
[11] A.P. Taylor, J. Izquierdo Reyes, L.F. Velásquez-García, Compact, magnetically actuated, additively manufactured pumps for liquids and gases, J. Phys. D Appl. Phys. 53 (35) (2020), https://doi.org/10.1088/1361-6463/ab8de8.
[12] A.K. Au, N. Bhattacharjee, L.F. Horowitz, T.C. Chang, A. Folch, 3D-printed microfluidic automation, Lab Chip 15 (8) (2015) 1934–1941, https://doi.org/10.1039/c5lc00126a.
[13] Y.S. Lee, N. Bhattacharjee, A. Folch, 3D-printed Quake-style microvalves and micropumps, Lab Chip 18 (8) (2018) 1207–1214, https://doi.org/10.1039/C8LC00001H.
[14] Q. Song, A. Hamza, C. Li, A.S. Sedeky, Y. Chen, M. Zhu, A. Goralczyk, F. Mayoussi, P. Zhu, P. Hou, C. Piesold, D. Helmer, B.E. Rapp, F. Kotz-Helmer, 3D printed elastic fluoropolymer with high stretchability and enhanced chemical resistance for microfluidic applications, Addit. Manuf. 81 (2024) 103991, https://doi.org/10.1016/j.addma.2024.103991.
[15] J. Huang, L. Zou, P. Tian, Q. Zhang, Y. Wang, J.-H. Zhang, A valveless piezoelectric micropump based on projection micro litho stereo exposure technology, IEEE Access 7 (2019) 77340–77347, https://doi.org/10.1109/access.2019.2919691.
[16] W. Qian, Z. Zhou, Q. Wang, W. Shi, M. Xu, D. Sun, The performance and fabrication of 3D variable cross-section channel for passive microfluidic control, Micromachines 15 (8) (2024) 1038, https://doi.org/10.3390/mi15081038.
[17] Q. Yan, Y. Yin, W. Sun, J. Fu, Advances in valveless piezoelectric pumps, Appl. Sci. 11 (15) (2021) 7061, https://doi.org/10.3390/app11157061.
[18] P. Patpatiya, K. Chaudhary, A. Shastri, S. Sharma, A review on polyjet 3D printing of polymers and multi-material structures, Proc. Inst. Mech. Eng. Pt. C. J. Mechan. Eng. Sci. 236 (14) (2022) 7899–7926, https://doi.org/10.1177/09544062221079506.
[19] M.M. Fadlelmula, B. Mazinani, V. Subramanian, Towards personalized microfluidics: 3D printing of high-performance micropumps by control and optimization of fabrication-induced surface roughness, Addit. Manuf. 94 (2024) 104468, https://doi.org/10.1016/j.addma.2024.104468.
[20] X. Wu, L. He, Y. Hou, X. Tian, X. Zhao, Advances in passive check valve piezoelectric pumps, Sens. Actuators A Phys. 323 (2021) 112647, https://doi.org/10.1016/j.sna.2021.112647.
[21] A.P. Taylor, L.F. Velasquez-Garcia, Miniaturized diaphragm vacuum pump by multi-material additive manufacturing, J. Micro Syst. 26 (6) (2017) 1316–1326, https://doi.org/10.1109/jmems.2017.2743020.
[22] C. Yamahata, C. Lotto, E. Al-Assaf, M.A.M. Gijs, A PMMA valveless micropump using electromagnetic actuation, Microfluid. Nanofluid 1 (3) (2004) 197–207, https://doi.org/10.1007/s10404-004-0007-6.
[23] S. Singh, N. Kumar, D. George, A.K. Sen, Analytical modeling, simulations and experimental studies of a PZT actuated planar valveless PDMS micropump, Sens. Actuators A Phys. 225 (2015) 81–94, https://doi.org/10.1016/j.sna.2015.02.012.
[24] R.R. Gidde, P.M. Pawar, B.P. Ronge, V.P. Dhamgaye, Design optimization of an electromagnetic actuation based valveless micropump for drug delivery application, Microsyst. Technol. 25 (2) (2018) 509–519, https://doi.org/10.1007/s00542-018-3987-y.
[25] C. Yamahata, Magnetically Actuated Micropumps, EPFL, 2005.
[26] Chen Lin, Michail E. Kiziroglou, Eric M. Yeatman, Electromagnetic micropumps based on multi-material 3D printing, IEEE Power 2024 (2024) 279–282, https://doi.org/10.1109/PowerMEMS63147.2024.10814506.
[27] F.W. Mauldin, Jr, M.A. Haider, E.G. Loboa, R.H. Behler, L.E. Euliss, T.W. Pfeiler, C. M. Gallippi, Monitored steady-state excitation and recovery (MSSER) radiation force imaging using viscoelastic models, IEEE Trans. Ultrason. Ferroelectr. Freq. Control 55 (7) (2008) 1597–1610, https://doi.org/10.1109/TUFFC.2008.836.
[28] Q. Hao, S. Greenhalgh, The generalized standard-linear-solid model and the corresponding viscoacoustic wave equations revisited, Geophys. J. Int. 219 (2019) 1939–1947, https://doi.org/10.1093/gji/ggz407.
[29] W. Jin, Y. Guan, Q. Wang, P. Huang, Q. Zhou, K. Wang, D. Liu, A smart active phase-change micropump based on CMOS-MEMS technology, Sensors 23 (11) (2023) 5207, https://doi.org/10.3390/s23115207.
[30] M. Leuthner, O. Hayden, Grease the gears: how lubrication of syringe pumps impacts microfluidic flow precision, Lab Chip 24 (1) (2023) 56–62, https://doi.org/10.1039/d3lc00698k.
[31] H. Lu, S. Amara, K. Moussi, S. Benmbarek, A. Ainine, H. Fariborzi, 3D printed electromagnetic micropump for implantable drug delivery, IEEE ICCE 2022 (2022) 1–5, https://doi.org/10.1109/icce53296.2022.9730456.
[32] Y. Zhou, F. Amirouche, An electromagnetically-actuated all-PDMS valveless micropump for drug delivery, Micromachines 2 (3) (2011) 345–355, https://doi.org/10.3390/mi2030345.